Journal Pre-proof

Lateral buckling of the compressed edge of a beam under finite bending

Federico Oyedeji Falope, Luca Lanzoni, Angelo Marcello Tarantino

PII: S0997-7538(24)00153-0
DOI: https://doi.org/10.1016/j.euromechsol.2024.105373
Reference: EJMSOL 105373

To appear in: *European Journal of Mechanics / A Solids*

Received date : 9 February 2024
Revised date : 10 June 2024
Accepted date : 13 June 2024

Please cite this article as: F.O. Falope, L. Lanzoni and A.M. Tarantino, Lateral buckling of the compressed edge of a beam under finite bending. *European Journal of Mechanics / A Solids* (2024), doi: https://doi.org/10.1016/j.euromechsol.2024.105373.

Lateral buckling of the compressed edge of a beam under finite bending

Federico Oyedeji Falope[1], Luca Lanzoni[2], Angelo Marcello Tarantino[3]

June 10, 2024

[1]DIEF, Università di Modena e Reggio Emilia, via P. Vivarelli 10, 41125, Modena, Italy, e-mail: federicooyedeji.falope@unimore.it,

[2]DIEF, Università di Modena e Reggio Emilia, via P. Vivarelli 10, 41125, Modena, Italy, e-mail: luca.lanzoni@unimore.it,

[3]DIEF, Università di Modena e Reggio Emilia, via P. Vivarelli 10, 41125, Modena, Italy, e-mail: angelomarcello.tarantino@unimore.it

Abstract

This paper investigates the critical condition whereby the compressed edge of a beam subjected to large bending exhibits a sudden lateral heeling. This instability phenomenon occurs through a mechanism different from that usually studied in linear theory and known as flexural-torsional buckling. An experimental test device was specifically designed and built to perform pure bending tests on soft materials. Thus, the experimental campaign provides not only the moment-curvature behavior of beams of narrow rectangular cross section, but also information regarding the post-critical lateral buckling behavior. To study the local bifurcation phenomenon, an analytical model is proposed in which a field of small transversal displacements, typical of the linear stability of thin plates, is superimposed on the large vertical displacement field of an inflexed beam in the nonlinear elasticity theory. Furthermore, numerous numerical simulations through nonlinear FE analysis have been performed. Finally, the results provided by the different methods applied were compared and discussed.

Keywords: Finite elasticity; Equilibrium; Beam; Bending; Lateral buckling; Bending experiments.

1 Introduction

The elastic stability of slender beams, deflected in the plane of maximum stiffness, has been extensively investigated since the pioneering works by Prandtl

(1899)[1] [1] and Michell (1899) [2]. In these first studies, the *critical load* of beams of rectangular cross section, under various conditions of loading and end-support, was calculated.

In 1960, Cherry [3] presented test results in the form of bifurcation loads for beams in uniform bending, whose compression flanges had prematurely buckled locally. Cherry supported his experimental work with a theoretical analysis based on the lateral stability. The interaction in thin-walled beams between local and lateral buckling was subsequently studied by Hancock et al. [4].

Several authors have extended the theory of lateral buckling of thin-walled beams by developing specific nonlinear analyses, including Reissner [5], Chang et al. [6], Machado [7], Attard and Kim [8]. Stability analysis of thick block subjected to large bending deformations were performed by Destrade et al. [9], [10], also showing onset of surface instabilities. FE analyses of lateral buckling were developed by Barsoum and Gallagher [11].

Fig. 1 illustrates the classic lateral buckling of an inflexed thin-walled[2] beam in the context of linearized elasticity. The beam is deflected in the vertical YZ-plane by couples M applied at the ends. In the initial phase, increasing M, the beam bends, with constant curvature (uniform bending) and the middle vertical plane of the beam always belongs to the YZ-plane. These equilibrium configurations are stable. Given the low transverse flexural stiffness, this situation can radically change when a critical value of M, denoted by M_{cr}, is reached. Indeed, when exceeding M_{cr}, the beam can deform laterally assuming (randomly) one of the two possible buckled configurations (as shown in Fig. 1b). In this circumstance, it is important to note that the unbuckled vertical configuration becomes unstable, while the two other adjacent buckled configurations are stable.

With reference to any intermediate section, the external vector moment $M\mathbf{i}$ (where $\mathbf{i}$ is the unit vector in the direction of the X axis) can be decomposed into three components evaluated along the ξ, η and ζ directions (cf. Fig. 1b and 1c). The tangent component to the deformed axis, along the ζ direction, is a torsion moment and is responsible for the global rigid rotation of the cross section, as shown by Fig. 1c. For this reason, the stability problem considered is often known as flexural–torsional buckling.

Once the three components of the vector moment according to the coordinate axes ξ, η and ζ have been calculated, a system of three differential equilibrium equations can be written in terms of the corresponding curvatures and twist.[3] Rearranging this system, the governing equation for the angle of twist $\beta(Z)$ is obtained. This equation has a mathematical structure very similar to the differential equation for the buckling of compressed beams (from which Euler's

[1] Ludwing Prandtl studied mechanical engineering at the Technische Hochschule (TH) in Münich and became an assistant of A. Föppl, who was also his doctoral tutor. Prandtl addressed the lateral buckling problem of beams in his thesis, the title of which was: *On Tilting Phenomena, an Example of Unstable Elastic Equilibrium* [1].

[2] Mechanically, a thin-walled beam, unlike a beam with a solid cross sectional area, is more prone to lateral buckling.

[3] In these equations, displacements and angle of twist $\beta(Z)$ are considered very small.

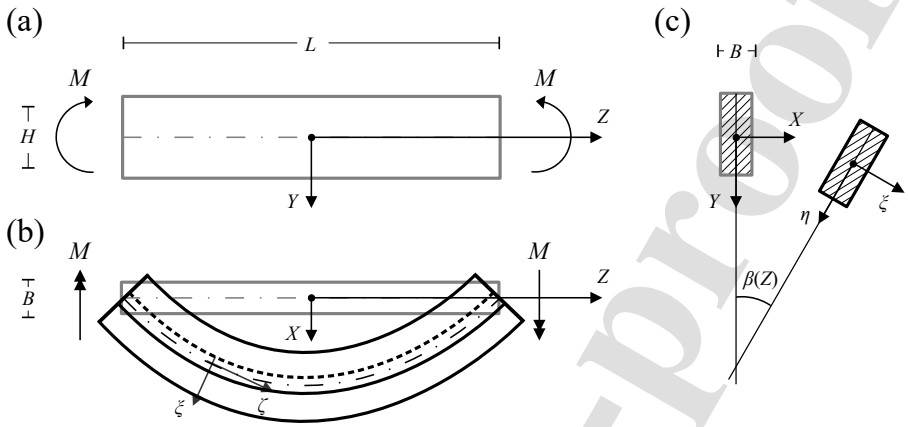

Figure 1: Lateral buckling of a hinged-hinged slender beam. (a) Initial rectilinear configuration. (b) Shape assumed after lateral buckling. (c) Rigid rotation of a generic cross section.

formula was derived) and gives the following critical value [12]:

$$M_{cr} = \frac{\pi\sqrt{B_Y C}}{L}, \tag{1}$$

which represents the smallest value of M at which buckling occurs. In the previous equation, $B_Y = \frac{HB^3}{12}E$ is the principal flexural rigidity in the YZ plane, and $C = \frac{HB^3}{3}\left(1 - 0.63\frac{B}{H}\right)G$ is the torsional rigidity[4], where E denotes the Young's Modulus and G the shear modulus. From formula (1), it can be seen that M_{cr} depends on the product of the smallest flexural rigidity B_Y and the torsional stiffness C, but does not depend on the flexural stiffness $B_X = \frac{BH^3}{12}E$. This is due to the fact that the vertical displacements are small as the flexural rigidity B_X is high.

In this paper, the same buckling problem illustrated by Fig. 1 is studied in the fully nonlinear context of finite elasticity. It is shown how the lateral buckling for the beam can occur due to a substantially different mechanism than the one described above. The intermediate cross sections do not only undergo a global rigid rotation, but starting from the compressed edge they also exhibit an important pure deformation, which shows how the lateral buckling is mainly localized at the upper edge of the beam. In fact, the corresponding transversal displacement field decreases quite quickly going towards the tensile part of the beam. Compared to the case of the linearized theory, the displacement field,

[4]The torsional rigidity C was calculated by Timoshenko and Goodier [13] in the case of narrow rectangle cross sections. In particular, to evaluate the constant 0.63, a logarithmic series, that converges very quickly, was assigned to the stress function (see eq. (161) on page 278 of [13]).

strains and stresses at each point of the beam change, but, above all, it is different the critical moment that produces the lateral buckling. After having formulated the lateral buckling for beams in finite elasticity, the comparison between the results provided by the two theories is performed.

In the next Section 2, experimental evidences of lateral buckling for beams capable of undergoing both large deformations and displacements are illustrated.

2 Experimental evidences

Experimental tests on lateral buckling of a beam are carried out reproducing a pure bending device that is able to impart a prescribed rotation at the final cross sections. This new device does not apply shear or axial forces to the specimen and was built inspired by the prototype presented in [14], which was designed to impart a prescribed rotation, but without the ability to perform mechanical measurements. Otherwise, the new prototype is equipped with load cells, which indirectly supply the reactive bending moment M associated with the prescribed angle α_0 (cf. Fig. 6b).

The new test machine is shown in Fig. 2. An external steel frame encloses the entire device, which is composed of an actuator that pushes up the contrast beam (brown beam in the bottom of Fig. 2 and sketched in Fig. 3a). The lower beam is restrained with two vertical slides placed at the beam edges. These slides constrain the vertical motion of the contrast beam along the vertical bars who act as guides (see Fig. 3b). A load cell is positioned between the two coupled blocks that compose the vertical slide. The load cells, symmetrically positioned in the device, support the lower beam (see Figs. 2 and 3b). Thus, the vertical motion of the actuator lifts the lower beam through the contrast beam. During this motion, the load cells read the vertical forces applied to the lower beam. Over the lower beam, a horizontal guide is fixed and equipped with two horizontal linear slides. The same components (i.e., the lower beam with a horizontal guide and linear slides) are fixed at the external steel frame in the upper part of the device (see Fig. 2). On each linear slide (four in total, two lower and two upper), the vertical masts of the pantograph are fixed. The masts are hinged with the diagonal arms of the pantograph. The diagonal arms of the pantographs extend a few centimeters beyond the inside part of the vertical masts (see Fig. 3c). On the extensions of the pantographs arms, the clamping system of the specimen is positioned (see Fig. 3c).

The operating principle of the device is the following: the vertical motion of the lower beam induces the closure of the pantographs, whose arms rotate around the hinged masts. The closure of the pantographs generates the horizontal sliding of the vertical masts mounted on the horizontal guides, letting free the final cross sections of the specimen to approach (see Fig. 4a). The rigid rotation of the pantographs arms is transferred to the final cross section of the specimen.

Because of the equilibrium conditions, the specimen is subjected to a couple

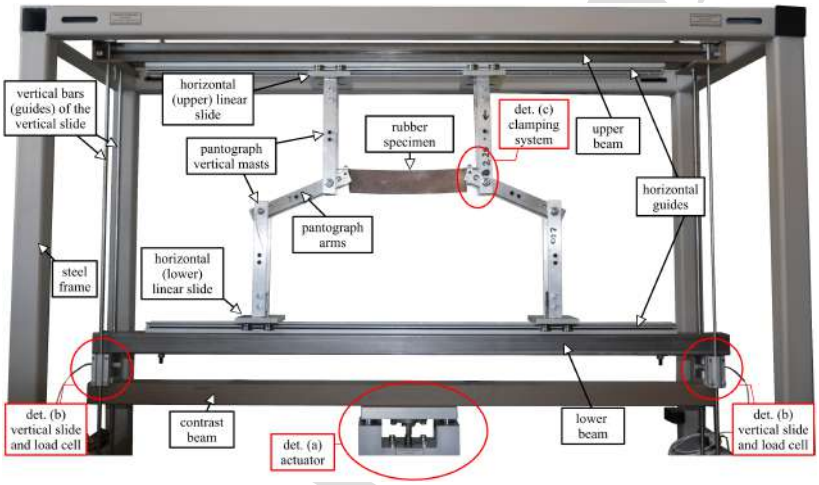

Figure 2: Device for pure bending test of soft materials. The operating principle is such that the approach of the lower beam, through the contrast bar pushed by the actuator, toward the upper beam generates the bending of the specimen. Between contrast beam and lower beam, two load cells (indirectly) measure the prescribed bending moment. Bending of the specimen is induced by the rotation of the pantograph arms which are hinged with the vertical masts. Vertical masts are coupled with the upper and lower beams through slides restrained to horizontal guides.

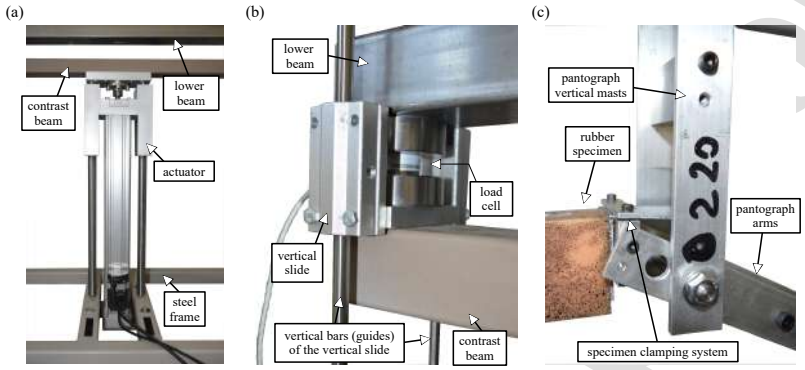

Figure 3: Details of bending device. (a) Actuator fixed at the external steel frame and connected with the moving contrast beam. (b) Detail of the two blocks composing the vertical slide and load cell positioning between the contrast beam and the lower beam. (c) Specimen clamping system and patterned surface monitored with the optical cameras (DIC).

of equal and opposite bending moments $M = F\,L_d\cos\omega(\alpha_0)$, being F the average force read by the load cells ($2F = F_1 + F_2$), L_d the distance between the hinge of the diagonal arm of the pantograph, and $\omega(\alpha_0)$ the inclination angle of the diagonal arms (cf. Fig. 4b).

The DIC optical cameras are positioned in front of the device. DIC positioning is such to monitor the prescribed twisting angle α_0 and both upper and frontal surfaces of the rubber specimen (see Fig. 5). DIC is used in stereo mode (two cameras). Thus, the entire 3D displacement filed has been acquired, in-plane and out-of-plane components.

3 Kinematics of beams subjected to finite bending

Based on a three-dimensional model, the finite bending of a beam was recently investigated in [15], [16] and [17]. We will start from the solutions presented in these papers to get the geometry of the deformed configuration of a beam, with a narrow rectangular cross section, subjected to a uniform bending moment. The problem is similar to the one illustrated in Fig. 1, with the fundamental difference that now both deformations and displacements can be large.

The longitudinal inflexion of the beam is generated by the application of a pair of self-balanced bending moments or, equivalently, by a geometric boundary condition which imposes a prescribed relative rotation between the two end faces of the beam (cf. Fig. 6b). In the latter case, the longitudinal curvature imparted to the beam is measured by the angle α_0. The longitudinal radius of curvature,

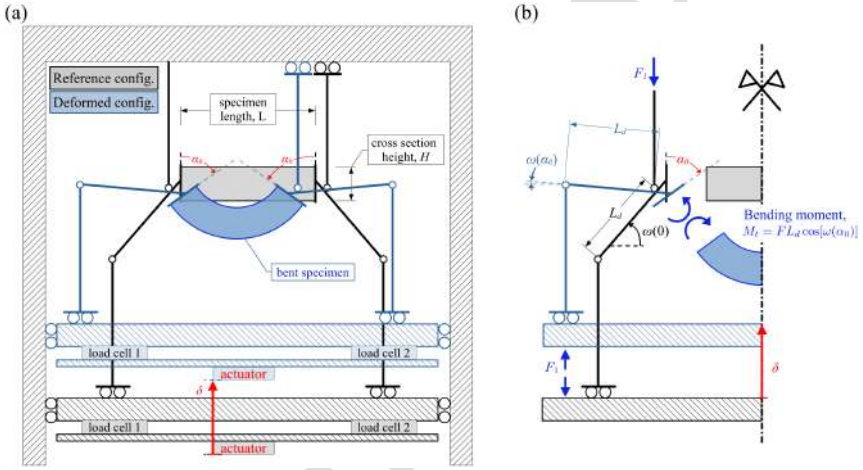

Figure 4: Static scheme of the pure bending device and computation of the bending moment. (a) Reference configuration (black tones), deformed configuration (blue tones), and kinematic control parameters activated by the actuator (red color). (b) Free body diagram of the device used to compute the (reactive) bending moment M from the acquisition of forces of the load cells.

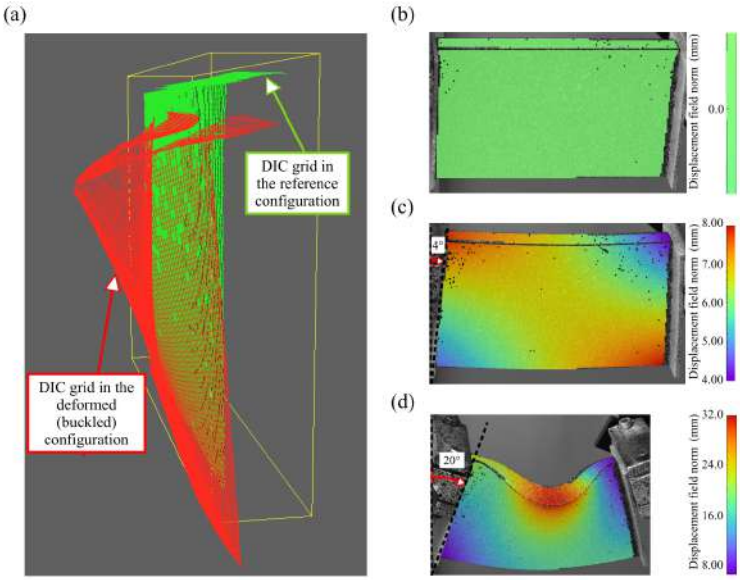

Figure 5: Pure bending test of the rubber specimen with evidence of lateral buckling acquired with the digital image correlation (DIC) cameras. (a) Data grid of the DIC in the reference configuration (green grid) and deformed configuration (red grid). (b), (c) and (d) Norm of the displacement field at $\alpha_0 = 0, 4, 20°$, respectively.

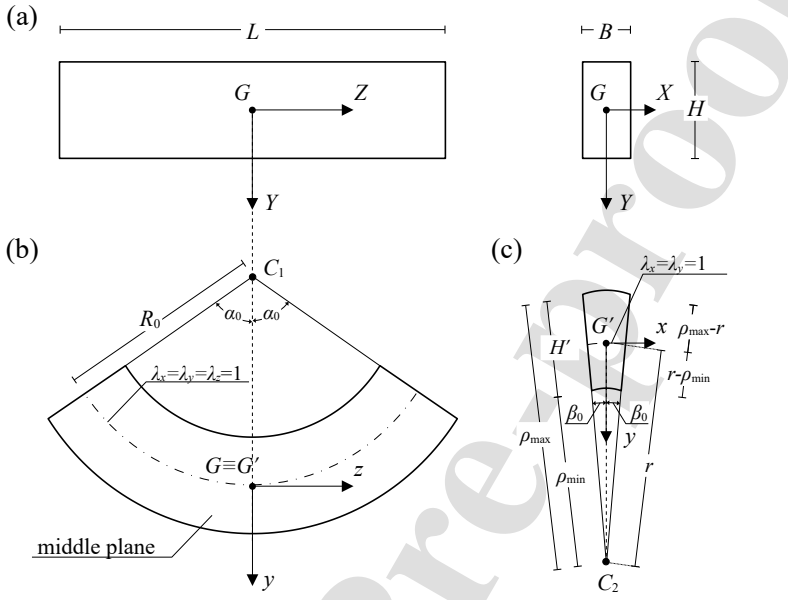

Figure 6: Geometric details of a beam under finite bending. (a) Undeformed configuration. (b) Deformed longitudinal section. (c) Deformed cross section.

R_0, and the transversal one, r, due to the anticlastic effect, are equal to [16]

$$R_0 = \frac{L}{2\alpha_0} \quad \text{and} \quad r = \frac{B}{2\beta_0} = R_0 \frac{a+3b+2c}{b+c}. \tag{2}$$

The radius R_0 is given by the geometric boundary condition, while the radius r is assessed by imposing the equilibrium conditions. In the expression of r appear the material constants a, b and c of the stored energy function ω in the form for compressible suggetio-Rivlin materials [18], [19]

$$\omega\left(I_1,\, I_2,\, I_3\right) = aI_1 + bI_2 + cI_3 - (a+2b+c)\ln I_3, \tag{3}$$

where I_1, I_2 and I_3 are the the principal invariants of the Cauchy-Green deformation tensors. Once the two radii R_0 and r have been defined, the Lagrangian stretches can be evaluated at each point of the beam (eq. (9) of [16]))

$$\begin{cases} \lambda_X = \lambda_Y = e^{-\frac{Y}{r}}, \\ \lambda_Z = 1 + \frac{r}{R_0}\left(1 - e^{-\frac{Y}{r}}\cos\frac{X}{r}\right). \end{cases} \tag{4}$$

Using (4), all the geometrical characteristics of the inflexed beam can be evaluated. The transverse radii ρ_{min} and ρ_{max}, shown in Fig. 6c, hold

$$\begin{cases} \rho_{min} = r - \int_0^{H/2} \lambda_Y(Y)\, dY = r\, e^{-\frac{H}{2r}}, \\ \rho_{max} = r + \int_{-H/2}^{0} \lambda_Y(Y)\, dY = r\, e^{\frac{H}{2r}}. \end{cases} \tag{5}$$

After deformation, the height H becomes

$$H' = \int_{-H/2}^{H/2} \lambda_Y(Y)\, dY = r\left(e^{\frac{H}{2r}} - e^{-\frac{H}{2r}}\right) = \rho_{max} - \rho_{min}. \tag{6}$$

With reference to the vertical middle plane ($x = 0$), the height H' can be divided into two segments of different lengths: $\rho_{max} - r = r\left(e^{\frac{H}{2r}} - 1\right)$ and $r - \rho_{min} = r\left(1 - e^{-\frac{H}{2r}}\right)$, which characterize the heights of the compressed and tensioned part of the beam.

Deformation transforms the width B into arcs that depend on variable Y (cf. Fig. 6c)

$$B'(Y) = \int_{-B/2}^{B/2} \lambda_X(Y)\, dX = B\, e^{-\frac{Y}{r}}. \tag{7}$$

From this expression some particular values are obtained: $B'(-\frac{H}{2}) = B\, e^{\frac{H}{2r}}$, $B'(0) = B$ and $B'(\frac{H}{2}) = B\, e^{-\frac{H}{2r}}$.[5]

All straight longitudinal fibers, parallel to the axis of the undeformed beam ($X = Y = 0$), become arcs of circle. In the middle plane ($X = 0$), the length of these longitudinal arcs can be evaluated as follows (cf. Fig. 6b):

$$L'(Y) = \int_{-L/2}^{L/2} \lambda_Z(0, Y)\, dZ = L\left(1 + \frac{r}{R_0}\left[1 - e^{-\frac{Y}{r}}\right]\right). \tag{8}$$

From this expression some particular values are obtained: $L'(-\frac{H}{2}) = L\left(1 + \frac{r}{R_0}\left[1 - e^{\frac{H}{2r}}\right]\right)$, $L'(0) = L$ and $L'(\frac{H}{2}) = L\left(1 + \frac{r}{R_0}\left[1 - e^{-\frac{H}{2r}}\right]\right)$.[6] $L'(-\frac{H}{2})$ is the length of the top edge and $L'(\frac{H}{2})$ of the bottom edge of the beam in the deformed configuration.

Substantially, the middle plane of the beam assumes the shape of an annulus sector, with the center of radial symmetry the pole C_1 of Fig. 6b. Meaning that along any radial direction, the cross sections all have the same geometric shape, stretches and stresses.

For the center line of the middle plane ($x = z = 0$), the law of transformation of the Lagrangian variable Y into the corresponding Eulerian y assumes the

[5] The same values can be calculated using the arc length formula: $B'(-\frac{H}{2}) = \rho_{max} 2\beta_0 = B\, e^{\frac{H}{2r}}$, $B'(0) = r\, 2\beta_0 = B$ and $B'(\frac{H}{2}) = \rho_{min} 2\beta_0 = B\, e^{-\frac{H}{2r}}$.

[6] The same values can be calculated using the arc length formula: $L'(-\frac{H}{2}) = [R_0 - (\rho_{max} - r)]\, 2\alpha_0 = L\left(1 + \frac{r}{R_0}\left[1 - e^{\frac{H}{2r}}\right]\right)$, $L'(0) = R_0\, 2\alpha_0 = L$ and $L'(\frac{H}{2}) = [R_0 + (r - \rho_{min})]\, 2\alpha_0 = L\left(1 + \frac{r}{R_0}\left[1 - e^{-\frac{H}{2r}}\right]\right)$.

following simple form (eq. (17) of [16]):[7]

$$y = r\left(1 - e^{-\frac{Y}{r}}\right). \tag{9}$$

Substituting (9) in (4), the Eulerian stretches for $X = x = 0$ are obtained

$$\begin{cases} \lambda_x = \lambda_y = \lambda = 1 - \frac{y}{r}, \\ \lambda_z = 1 + \frac{y}{R_0}, \end{cases} \tag{10}$$

which can be used to evaluate the longitudinal Cauchy principal stresses (eq. (28) of [16])

$$T_3 = \frac{2}{\lambda^2 \lambda_z}\left\{\left(\lambda_z^2 - 1\right) a + 2\left(\lambda^2 \lambda_z^2 - 1\right) b + \left(\lambda^4 \lambda_z^2 - 1\right) c\right\}. \tag{11}$$

Given the radial symmetry, the stretches (10) and stresses (11), evaluated for vertical middle plane, are the same along every straight line outgoing from pole C_1.

4 Formulation and resolution of the stability problem

In the previous Section, the geometrical characteristics of a beam with a rectangular cross section under finite bending were illustrated, describing the shape assumed by the beam in the deformed configuration. The vertical middle plane of the beam transforms into the annulus sector shown in Fig. 7. Considering the radial symmetry, to represent any point P on this plane it is convenient to introduce a system of polar coordinates, with pole C_1, radius $\rho \in [\rho_{min}, \rho_{max}]$ and polar angle $\vartheta \in [-\alpha_0, \alpha_0]$. The same figure shows the principal Cauchy stress distributions (11), which have as resultant two self-equilibrated bending couples M.

From the situation illustrated in Fig. 7, the aim is now to identify a critical value of the angle α_0 for which lateral buckling becomes incipient (as can be seen from Fig. 6, the angle α_0 is half the angle of relative rotation between the two end cross sections of the beam). Lateral buckling manifests itself with the appearance of an additional displacement field $u(\rho, \vartheta)$, orthogonal to the middle plane, which, as seen in Section 2, has the shape similar to a semi-wave at the upper compressed edge, whose amplitude quickly decreases as the radius ρ grows. Obviously, in the absence of this displacement field $u(\rho, \vartheta)$, there is no lateral buckling.

To model the stability problem, a small orthogonal displacement field, which has the role of a perturbation of the equilibrium solution, is superimposed on the large vertical displacement generated by the nonlinear bending of the beam.

[7] That is to say that, while in the undeformed configuration $Y \in [-H/2, H/2]$, in the deformed configuration the corresponding $y \in \left[-r\left(e^{\frac{H}{2r}} - 1\right), r\left(1 - e^{-\frac{H}{2r}}\right)\right]$ (cf. Fig. 6c).

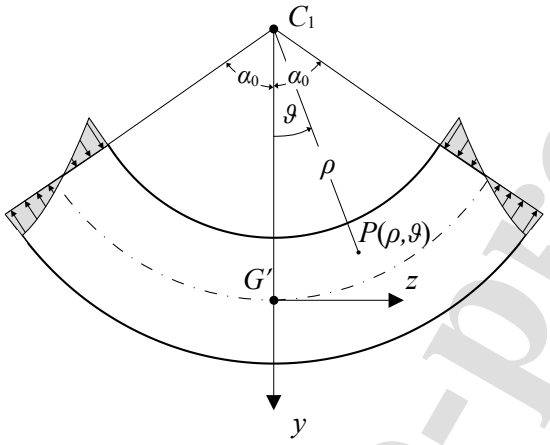

Figure 7: The vertical middle plane of the beam in the deformed configuration.

Being small, this orthogonal displacement field can be evaluated using the linearized elasticity theory. Namely, starting from the deformed configuration shown in Fig. 7, a small increase in the lateral displacements is added, assuming that this lateral deflection surface has a shape similar to that highlighted by the experimental tests (cf. Fig. 5). Then, the magnitude that the Cauchy stresses (caused by the prescribed angle α_0) must have in order to keep the middle plane in such a slightly buckled shape is calculated. Instability therefore occurs when the (linear) perturbed equilibrium problem admits the solution $u(\rho, \vartheta)$.

Methods for stability analysis, known in the literature, can be used to calculate the above critical load. To evaluate the lateral displacement field $u(\rho, \vartheta)$, the deformed beam is now assimilated to a (linear) plate [8], in the shape of an annulus sector, loaded solely in its own plane by the Cauchy stresses (11). Using the polar coordinates, the differential equation for the buckled plate is [9]

$$\left(\frac{\partial^2}{\partial\rho^2}+\frac{1}{\rho}\frac{\partial}{\partial\rho}+\frac{1}{\rho^2}\frac{\partial^2}{\partial\vartheta^2}\right)\left(\frac{\partial^2 u}{\partial\rho^2}+\frac{1}{\rho}\frac{\partial u}{\partial\rho}+\frac{1}{\rho^2}\frac{\partial^2 u}{\partial\vartheta^2}\right)=\frac{1}{D\rho^2}N_\vartheta\left(\frac{\partial^2 u}{\partial\vartheta^2}+\rho\frac{\partial u}{\partial\rho}\right), \tag{12}$$

where $D=\frac{EB^3}{12(1-\nu^2)}$ and $N_\vartheta = T_3\,B$ is the normal forces per unit length. In both these terms, the thickness B can be considered constant, because it substantially undergoes a very small variation, being r much larger than Y (cf. eq. (7)). The symbol E denotes the Young's modulus and ν the Poisson's ratio. The corresponding tangent values matured in the deformed configuration of the beam must be assigned to these two constitutive parameters.[10] To evaluate T_3,

[8] In linearized elasticity, a similar approach was proposed by Reissner [20].

[9] Since beams with narrow rectangular cross sections are considered, Kirchhoff plate theory is applied.

[10] In the case of infinitesimal deformations, the compressible Mooney-Rivilin law reproduces

variable y can be replaced with the radial radius ρ in (10) and these in turn introduced in (11).

Boundary conditions must be added to the field equation (12). Taking into account the shape of the lateral deflection surface, these, for the short sides, are

$$u = \frac{\partial u}{\partial \vartheta} = 0, \text{ for } \quad \vartheta = \pm\alpha_0. \tag{13}$$

For the upper edge the bending moment and the shearing force are null, since the side $\rho = R_{min} = R_0 + r\left(1 - e^{\frac{H}{2r}}\right)$ is free. In kinematic terms these conditions become

$$\begin{cases} \frac{\partial^2 u}{\partial \rho^2} + \frac{\nu}{\rho}\frac{\partial u}{\partial \rho} + \frac{\nu}{\rho^2}\frac{\partial^2 u}{\partial \vartheta^2} = 0, \\ \frac{\partial(\nabla u)}{\partial \rho} + \frac{(1-\nu)}{\rho^2}\left[\frac{\partial^3 u}{\partial \rho \partial \vartheta^2} - \frac{1}{\rho}\frac{\partial^2 u}{\partial \vartheta^2}\right] = 0, \end{cases} \tag{14}$$

with $\nabla u = \frac{\partial^2 u}{\partial \rho^2} + \frac{1}{\rho}\frac{\partial u}{\partial \rho} + \frac{1}{\rho^2}\frac{\partial^2 u}{\partial \vartheta^2}$. At the bottom edge, that is the side with $\rho = R_{max} = R_0 + r\left(1 - e^{-\frac{H}{2r}}\right)$, the same boundary conditions apply.

However, the boundary value problem, formulated by the field equation (12) and boundary conditions (13) and (14), is difficult to solve, since the lateral load N_ϑ is variable in ρ and, consequently, the differential equation (12) has variable coefficients. In this situation, the energetic method can be conveniently applied in investigating buckling of plates, and also to assess an approximate value of the critical load [12]. This method assumes that the plate undergoes some small out-of-plane bending consistent with the boundary conditions. Such small bending can be produced without stretching the middle plane. The critical forces, for which the flat form of the plate becomes unstable and lateral buckling occurs, can be evaluated by equating the variation of strain energy of bending, δU, for every possible shape of lateral buckling, to the variation of work done by external forces acting in the middle plane of the plate, δL. These energies have the following expressions:

$$\delta U = \frac{D}{2}\int_{-\alpha_0}^{\alpha_0}\int_{R_{min}}^{R_{max}} \left(\frac{\partial^2 u}{\partial \rho^2} + \frac{1}{\rho}\frac{\partial u}{\partial \rho} + \frac{1}{\rho^2}\frac{\partial^2 u}{\partial \vartheta^2}\right)^2 - 2(1-\nu)\frac{\partial^2 u}{\partial \rho^2}\left(\frac{1}{\rho}\frac{\partial u}{\partial \rho} + \frac{1}{\rho^2}\frac{\partial^2 u}{\partial \vartheta^2}\right) + 2(1-\nu)\left(\frac{1}{\rho}\frac{\partial^2 u}{\partial \vartheta \partial \rho} - \frac{1}{\rho^2}\frac{\partial u}{\partial \vartheta}\right)^2 \rho \, \partial\rho \, \partial\vartheta, \tag{15}$$

$$\delta L = \frac{1}{2}\int_{-\alpha_0}^{\alpha_0}\int_{R_{min}}^{R_{max}} N_\vartheta \left(\frac{1}{\rho}\frac{\partial u}{\partial \vartheta}\right)^2 \rho \, \partial\rho \, \partial\vartheta. \tag{16}$$

To apply the energy method, the general expression of $u(\rho, \vartheta)$, which satisfies the boundary conditions (13) and (14), can be taken in the following form

---

the classic linear constitutive one with [15]

$$\begin{cases} E = \frac{4(a+b)(a+4b+3c)}{a+3b+2c} \\ \nu = \frac{b+c}{a+3b+2c}. \end{cases}$$

of an infinite trigonometric series:

$$u\left(\rho,\,\vartheta\right)=\sum_{m,n}a_{mn}\left(1+b_m\cos\frac{m\pi}{R_{max}}\rho+c_m\sin\frac{m\pi}{R_{max}}\rho\right)\left(1+\cos\frac{n\pi}{\alpha_0}\vartheta\right), \tag{17}$$

where the constants a_{mn}, b_m and c_m will be determined depending on the specific case studied. As is known in stability problems, the solution is always determined to less than a multiplicative constant.

5 Numerical analysis

Following a numerical approach, finite element simulations are performed using the finite element code COMSOL Multiphysics® v.6.1. The compressible Mooney-Rivlin law (see eq. (3)) is implemented by using the principal stretches variables of the finite element code. The beam subjected to finite bending is modeled using brick elements, with aspect ratio of 1, and characterized by cubic serendipity shape functions. This first approach numerically models lateral buckling in a fully nonlinear context.

Specifically, the first FE analysis consists of an incremental procedure where the kinematic control parameter of the analysis is the prescribed rotation at the final cross section of the beam. The lateral heeling of the beam is investigated by introducing a geometrical imperfection of the beam. The beam is modeled by extruding the transversal cross section along the cosinusoidal axes of the beam (see Fig. 8). The amplitude A of the cosinusoidal axis represents the imperfection which allows us to look for the buckled configuration as a stable configuration. We have assumed a negligible imperfection: $A = L/5000$. The objective of this small imperfection is to best simulate the results provided by the experimental tests.

The second numerical approach consists of a linear buckling analysis. The objective of this second analysis is to numerically compare the nonlinear solution with the classical linear one. In this second FE analysis, the beam is modeled as a linear elastic parallelepiped with rectilinear axis (the above imperfection has been removed) and we proceed as in a classical eigenvalue problem, after having defined Young's modulus and Poisson's ratio consistent with the Mooney-Rivlin material. A unitary bending moment resultant is applied to the final cross sections of the beam.[11] Thus, the first critical load factor provided by the code COMSOL represents the critical bending moment.

6 Comparisons

In this Section, three different approaches (analytical, numerical and experimental) are applied to solve the lateral buckling problem and the results obtained are compared and discussed.

[11] For details regarding aspects of FE modeling see Section 5 of [18].

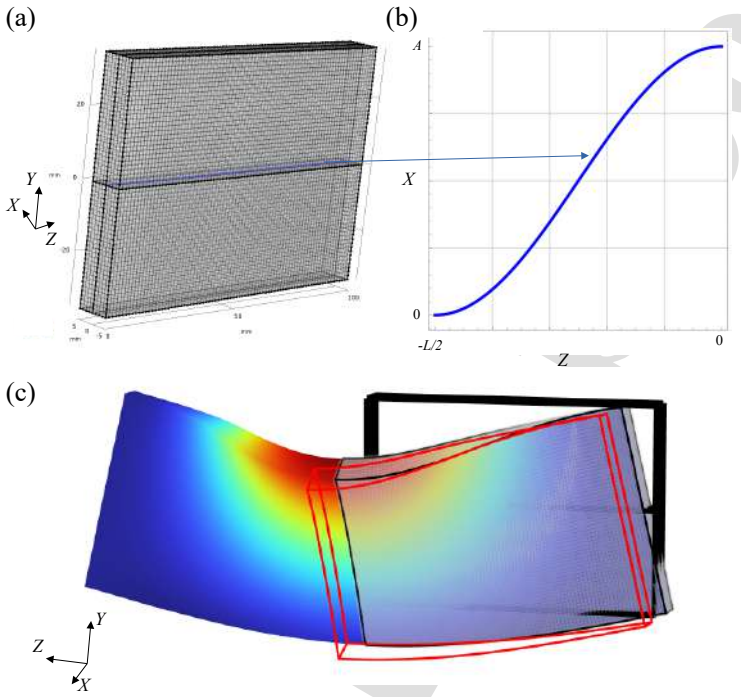

Figure 8: Deformed shape of the bent beam subjected to prescribed rotations at the ends. (a) FE mesh. (b) deformed shape along Z direction for the fiber $X = Y = 0$. (c) 3D sketch of the deformed shape for different values of the angle α_0.

For a beam under finite uniform bending, the critical value of the angle α_0 for which lateral buckling becomes incipient is evaluated with the energy method proposed in the previous Section 4, which superimposes to the large displacement field of a deformed beam under finite bending (cf. Section 3) a small perturbation constituted by the small displacement field of linear stability problems of deflected plates.

Discrete investigations concerning specific prismatic samples were performed through experimental trials carried out with a specifically designed testing machine, whose operation has been described in Section 2. For the experimental tests, three beam samples with heights $H = 50$, 60 and 70 [mm], width $B = 10$ [mm] and length $L = 200$ [mm], are considered.

The material used for the experiments is a Neoprene rubber. The uniaxial characterization of the material has led to the following constitutive parameters: $a = 554.9$, $b = 523.4$ and $c = 11938$ [kPa].

As reported in Section 4, an upper bound estimation of the critical angle

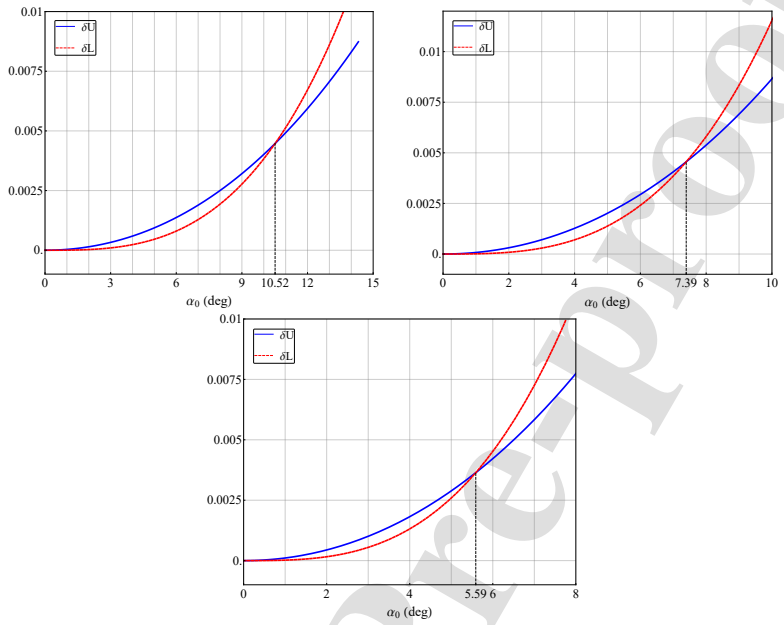

Figure 9: Curves of the strain energy and external work varying the angle α_0 for the samples with $H = 50$, 60 and 70, $B = 10$ and $L = 200$ [mm].

α_{CR}, that causes the buckling of the system, is the value of this angle that rends the variation of the strain energy (15) equals to the variation of the external work (16), based on the out-of-plane perturbation assumed in compliance with expression (17). Such a calculation has been performed by truncating the series expansion (17) to the first terms. In particular, it is found that good approximations are obtained by assuming only three terms of the series: a single term in the ϑ coordinate and two in the ρ coordinate, namely:

$$u(\rho, \vartheta) = \left(1 + b_1 \cos \frac{\pi}{R_{max}} \rho + c_1 \sin \frac{\pi}{R_{max}} \rho\right) \left(1 + \cos \frac{\pi}{\alpha_0} \vartheta\right). \tag{18}$$

Constants b_1, c_1 have been found to make the solution a minimum through an iterative procedure. The starting values $b_1(0)$, $c_1(0)$ have been determined according to a best fitting procedure in such a way to resemble a rigid rotation of the cross section around $\rho = R_{max}$ (i.e., by assuming a linear dependence of displacement u on ρ coordinate). Based on such an approach, Fig. 9 have been obtained about the samples with $H = 50$, 60 and 70 [mm], thus finding $\alpha_{CR} = 10.52°$, $7.39°$ and $5.59°$.

As shown in Fig. 10a, the critical angle α_{CR} decreases as H increases. Note also that the gap between nonlinear FE and theoretical solutions decreases with H. This can be ascribed to the fact that the analytic formulation has

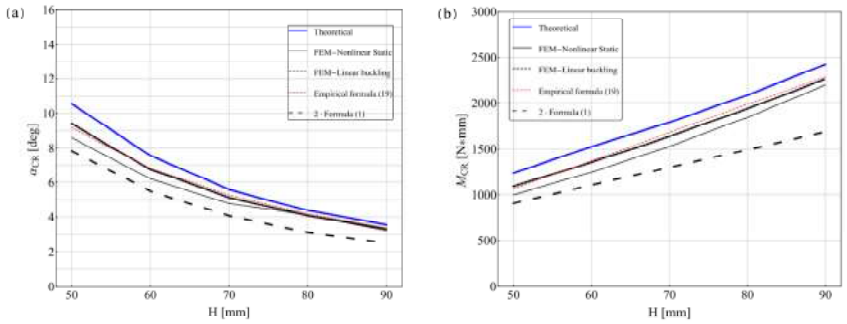

Figure 10: Comparison between theoretical and FE results. (a) Values of the critical angle α_{CR} varying the height H of the beam. (b) Values of the critical angle M_{CR} varying the height H of the beam. Note that, in compliance with the clamped-clamped condition, results provided by (1) have been doubled.

been based on the Kirchhoff-Love theory for thin plates, thus neglecting the shear deformations and other deformations in the thickness of the plates, which instead are taken into consideration by the nonlinear FE analysis based on brick elements. In any case, the difference between theoretical and FE results are not important, despite the fact that only few terms have been taken into account in expression (18). As shown in Fig. 10b, conversely to the critical angle α_{CR}, the critical bending moment M_{CR} increases as H increases due to the enhancement of the flexural rigidity with H. An almost linear trend of M_{CR} vs H is found, while the M_{CR}/α_{CR} ratio decreases as α_{CR} increases. In Fig. 10a and 10b, using a dotted curve, the values obtained from the application of the classic formula (1) are also shown. These values are multiplied by two to take into account the different constraint conditions at the ends of the beam: clamped-clamped instead of hinged-hinged. It can be noted that the values given by (1) are less accurate from the beginning and the approximation increases as H increases. This confirms that lateral buckling of thin-walled beams occurs with a critical mode different from that predicted by (1) derived in the framework of classical Euler-Bernoulli beam theory.

The main results provided by the numerical simulations based on the nonlinear incremental analyses are shown in Figs. 11-12. Fig. 11 shows the response of the samples subjected to an increasing value of the bending angle α_0. Fig. 11a shows the dimensionless bending moment as a function of dimensionless curvature, $\chi_0 L/2$, for the case of a beam of height 50, 60 and 70 mm, red, green and blue markers respectively. The choice of the adimensionalisation parameters is such that it provides a unitary slope corresponding with the linear elasticity (solid line), corresponding with the real linear Young modulus of the material obtained from uniaxial tests (E_{real}), while the dashed line represents the ratio between the real Young modulus and the Young modulus of the Mooney-Rivlin

material (E_{MR}) provided by the best-fit procedure of the uniaxial test. Since the best-fit of the Mooney-Rivlin material underestimates the real stiffness of the material, it can be noted that the use of nonlinear constitutive law will bring an underestimation of the critical bending moment of the Neoprene rubber. Under the linear segments, the grey region denotes the onset of bending instability as highlighted by the buckled deformed configuration grasped with the DIC optical monitoring (see the detail of Fig. 11a).

Figs. 11b-d show the bending moment as a function of the prescribed bending angle α_0 of the three investigated cases compared with the nonlinear static analysis of the FE models. Square markers denote experimental values, while the cross marker is used to distinguish the onset of instability, that is the point (α_{CR}, M_{CR}). Such values are reasonably chosen in correspondence to the first experimental value which deviates markedly from the initial trend. Likewise, the nonlinear static incremental analysis, denoted with continuous lines (FEM), exhibits a sudden change, which represents the bifurcation. Before bifurcation, FE models are overlapped with the linear trend supporting the negligibility of the imperfection introduced in the FE models. The values of the critical angles predicted by the buckling analysis of FE models and the theoretical approach of Section 4 are introduced with framed values in Figs. 11b-d, $\alpha_{CR,FEM\,Bk}$ and $\alpha_{CR,\,Th}$, respectively.

The comparison between the post-critical behaviour of the experiments and the nonlinear static analysis of the FE models is reported in Fig. 12. This comparison is done in terms of out-of-plane displacement of the point $P_1(0, H/2, 0)$, shown on the right side of the Fig. 12. Experiments, denoted with square markers, exhibit a progressive lateral heel since the beginning of the tests. This suggests the presence of an imperfection of the specimens axes. For this reason, Fig. 12 reports the behaviour of the lateral heeling of two different nonlinear FE models characterized by two different imperfections: $A = L/5000$ (continuous line) and $A = L/200$ (dashed lines). The smallest and negligible imperfection deviates significantly from the lateral heel observed during tests. Conversely, the greatest imperfection shows a good agreement suggesting the presence of an imperfection on the Neoprene specimens of the order of 1 mm.

To summarize the results obtained, Table 1 reports the values of the critical angle α_{CR} provided by the three different approaches. As already mentioned, the theoretical approach provides an upper bound of the critical bending angle. The experiments conducted on samples with small aspect ratios H/B are a little less suitable for describing the problem studied. As the height H of the specimens increases, a substantial convergence of the results is observed.

6.1 Approximate formula

The shape of the deformed configuration in the planes normal to the Y direction (ZX planes) resemble the first buckling mode of a linear beam clamped at both ends. This suggests a way to obtain an empirical estimation of the critical angle α_{CR}. In particular, considering the critical load of a beam fixed at both ends

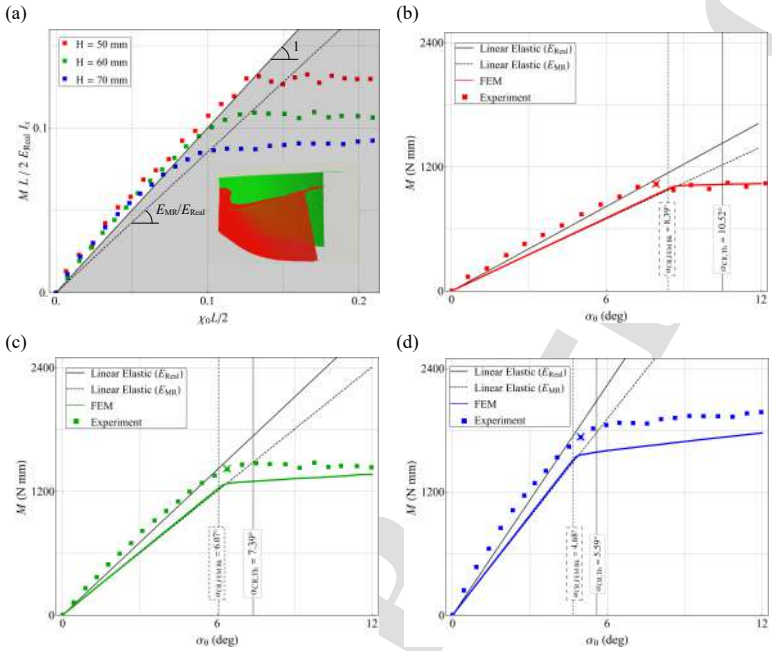

Figure 11: Experimental flexural behavior and comparison with the linear case. (a) Experimental response of the bent samples in terms of moment-curvature curves. (b) Experimental moment-bending angle α_0 curve for the sample with $H = 50$ mm. (c) Experimental moment-bending angle α_0 curve for the sample with $H = 60$ mm. (d) Experimental moment-bending angle α_0 curve for the sample with $H = 70$ mm.

H (mm)	Experimental	FEM (NL st.)	Theoretical
50	7.95	8.60	10.52
60	6.40	6.20	7.39
70	4.93	4.80	5.59

Table 1: Values of the critical angles α_{CR} (in deg), obtained from experiment analysis, FEM using the nonlinear incremental static analysis with an initial imperfection and theoretical formulation.

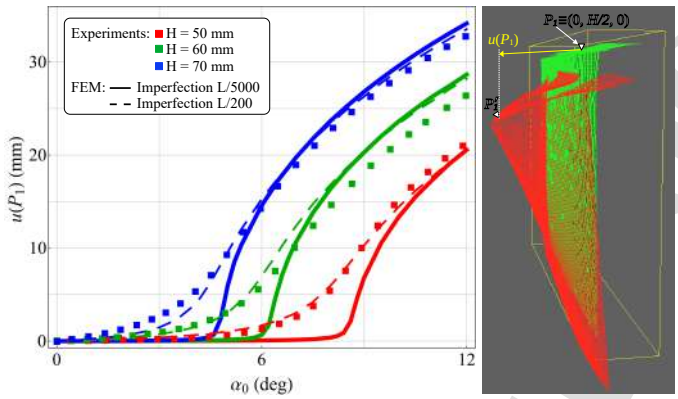

Figure 12: Out-of-plane horizontal displacement of point P_1 of the bent samples versus the angle of rotation α_0 at the ends. Comparison among experimental (discrete points) and FE results (dashed and solid lines).

with length L, and equating the width of the beam with h^* one finds

$$\alpha_{CR} \simeq \frac{\pi^2 B^2}{3L\,(H - h^*)}, \tag{19}$$

where $h^* \in (0.7H, 0.8H)$. A good approximation of the critical angle is achieved by taking $h^*/H \simeq 0.77$. Such an empirical formula has been used to obtain the curve labelled as "empirical formula" in Fig. 10. With the same degree of approximation, the M_{CR} values shown in Fig. 10b have been obtained by multiplying the α_{CR} values provided by (19) by the bending stiffness $2EI_X/L$, where I_X and L are the moment of inertia of the cross section about the X axis and the length of the undeformed beam, while the Young's modulus E is the corresponding elastic modulus of a Mooney-Rivlin material reported in the footnote (10).

7 Conclusions

In this paper, the problem of lateral buckling of a beam inflexed in finite elasticity has been investigated. The possibility that the beam can undergo large deformations transforms the collapse mechanism compared to that of the classical linearized elasticity, where the intermediate cross sections exhibit only rigid rotation (flexural-torsional buckling). In finite elasticity, differently, the cross sections can deflect transversely, showing also pure deformation in addition to rigid rotation. In particular, starting from the compressed edge of the beam, an out-of-plane displacement field appears, which takes the form of a cosine half-wave that rapidly decreases moving towards the tensioned edge.

To study the problem from an experimental point of view, a special test machine was designed and built, and with it an extensive experimental campaign was carried out. The technical details of the test equipment were delivered in Section 2, while the most important results of the experimental analysis were reported, discussed and compared in Section 6.

To model the lateral buckling, a linear stability analysis was superimposed on the nonlinear bending problem. Specifically, starting from the deformed configuration of the beam, a very small lateral displacement field, similar to that highlighted by the experimental tests, was added. Then, the magnitude that acting Cauchy stresses must reach to move the beam out of the middle plane is calculated. Instability therefore occurs when the (linear) perturbed equilibrium problem admits a solution, namely a small displacement field orthogonal to the middle plane of the beam. Operationally, to compute the critical load the energy method was applied.

Following a numerical approach, the beam subjected to finite bending was studied by FE analyses with brick elements, characterized by cubic serendipity shape functions. The FE analysis consists of an incremental procedure, where the lateral heeling of the beam is investigated by introducing a geometrical imperfection of the beam. This nonlinear static incremental analysis exhibits a sudden change, which represents the bifurcation, and then reproduces the post-critical equilibrium path. For a useful comparison, linear buckling analyses were also performed.

All the methods applied, although of different types (analytical, numerical and experimental), provide comparable results.

Acknowledgment L.L. gratefully acknowledges financial support Italian Ministry of University and Research (MUR) through the research grant PRIN 2022 PNRR "New challenges of thin-walled structures at large strains and their promising applications" (prot. P2022AHFCP; CUP C53D23008220001). AMT gratefully acknowledges the financial support of the MUR through the research grant PRIN 2022 "New eco-friendly building materials inspired by ancient constructions" (prot. 2022Y2RHHT; CUP E53D23003900006); PRIN 2022 PNRR "Energy harvesting via naturally induced piezoelectric vibration with a view towards application" (prot. P2022ATTAR; CUP B53D23026940001).

References

[1] L. Prandtl. Kipperscheinungen. Dissertation der Univ. München (1899). In Ludwig Prandtl Gesammelte Abhandlungen, Erster Teil, Berlin, Springer-Verlag (1961) 10-74.

[2] A.G.M. Michell, Elastic stability of long beams under transverse forces. *Phil. Mag.* **48** (1899) 298-309.

[3] S. Cherry, The stability of beams with buckled compression flanges. *Struct. Eng.* **38** (1960) 277-285.

[4] G. J. Hancock, M. A. Bradford, N. S. Trahair, Web distortion and flexural torsional buckling. *J. Struct. Div., ASCE.* **106** (1980) 1557-1571.

[5] E. Reissner, Lateral buckling of beams. *Computers and Structures* **33** (1989) 1289– 1306.

[6] S.P. Chang, S.B. Kim, M.Y. Kim, Stability of shear deformable thin-walled space frames and circular arches. *J. of Eng. Mechanics* **122** (1996) 844–854.

[7] S. Machado, Non-linear buckling and postbuckling behavior of thin-walled beams considering shear deformation. *Inter. J. of Non-Linear Mechanics* **43** (2008) 345–365.

[8] M.M. Attard, M. Kim, Lateral buckling of beams with shear deformations – A hyperelastic formulation. *Inter. J. of Solids and Structures* **47** (2010) 2825–2840.

[9] M. Destrade, A. Ní Annaidh, C.D. Coman, Bending Instabilities of Soft Biological Tissues. *Inter. J. Solids Struct.* **46** (2009) 4322–4330.

[10] M. Destrade, M.D. Gilchrist, J.G. Murphy, Onset of Nonlinearity in the Elastic Bending of Blocks. *J. of Applied Mechanics* **77** (2010).

[11] R.S. Barsoum, R.H. Gallagher, Finite element analysis of torsional and torsional-flexural stability problems. *Int. J. for Numer. Meth. in Engin.* **2** (1970) 335-352.

[12] S. Timoshenko, *Theory of elastic stability*. McGraw-Hill Book Company, New York and London (1936).

[13] S. Timoshenko, J.N. Goodier, *Theory of elasticity*. McGraw-Hill Book Company, New York, Toronto and London (1951).

[14] F.O. Falope, L. Lanzoni, A. M. Tarantino, Bending device and anticlastic surface measurement of solids under large deformations and displacements. *Mechanics Research Communications* **97** (2019) 52–56.

[15] L. Lanzoni, A.M. Tarantino, Finite anticlastic bending of hyperelastic solids and beams. *J. Elasticity* **131** (2018) 137-170.

[16] L. Lanzoni. A.M. Tarantino. The bending of beams in finite elasticity. *J. Elasticity* **139** (2020) 91-121.

[17] F.O. Falope, L. Lanzoni, A. M. Tarantino, The bending of fully nonlinear beams. Theoretical, numerical and experimental analyses. *Inter. J. of Eng. Science.* **145** (2019) 103167.

[18] F.O. Falope, L. Lanzoni, A. M. Tarantino. Finite bending of non-slender beams and the limitations of the Elastica theory. *Inter. J. of Mech. Science* (2022) DOI: 10.1016/j.ijmecsci.2022.107187.

[19] M. Pelliciari, S. Sirotti, A.M. Tarantino, A strain energy function for large deformations of compressible elastomers. *J.Mech. Phys. Solids* (2023) 105308.

[20] E. Reissner, The Problem of Lateral Buckling of Cantilever Plates. *ZAMM. 2. angew. Math. Mech.* **75** (1995) 8, 615-621.

- We study the lateral buckling occurring in prismatic plate-like solids under finite bending.
- The onset of buckling is quantified through the energy criterion.
- A small out of plane small perturbation is superposed to the in-plane nonlinear displacement field induced by large bending.
- Upper bound of the critical curvature is found and compared with FE buckling analyses and experiments finding good agreement.

AUTHOR STATEMENT

Federico Oyedeji Falope: Data curation, investigation, formal analysis.

Luca Lanzoni: Conceptualization, investigation, review & editing.

Angelo Marcello Tarantino: Visualization, supervision, writing, methodology.

Declaration of interests

☒ The authors declare that they have no known competing financial interests or personal relationships that could have appeared to influence the work reported in this paper.

☐ The authors declare the following financial interests/personal relationships which may be considered as potential competing interests: